Journal of Microscopy

Journal of Microscopy, Vol. 261, Issue 1 2016, pp. 88–104
Received 29 April 2015; accepted 30 August 2015

doi: 10.1111/jmi.12319

Visualization of water drying in porous materials by X-ray phase contrast imaging

F. YANG*,†, M. GRIFFA*, A. BONNIN‡,§, R. MOKSO‡, C. DI BELLA*,†, B. MÜNCH*, R. KAUFMANN* & P. LURA*,†

*Empa, Swiss Federal Laboratories for Materials Science and Technology, Dübendorf, Switzerland

†Institute for Building Materials (IfB), Swiss Federal Institute of Technology Zurich (ETHZ), Zürich, Switzerland

‡Swiss Light Source, Paul Scherrer Institute, Villigen, Switzerland

§Center for Biomedical Imaging, Swiss Federal Institute of Technology Lausanne (EPFL), Lausanne, Switzerland

Key words. Image analysis, liquid transport, porous materials, X-ray phase contrast imaging, X-ray tomographic microscopy, water.

Summary

We present in this study results from X-ray tomographic microscopy with synchrotron radiation performed both in attenuation and phase contrast modes on a limestone sample during two stages of water drying. No contrast agent was used in order to increase the X-ray attenuation by water. We show that only by using the phase contrast mode it is possible to achieve enough water content change resolution to investigate the drying process at the pore-scale. We performed 3D image analysis of the time-differential phase contrast tomogram. We show by the results of such analysis that it is possible to obtain a reliable characterization of the spatial redistribution of water in the resolved pore system in agreement with what expected from the theory of drying in porous media and from measurements performed with other approaches. We thus show the potential of X-ray phase contrast imaging for pore-scale investigations of reactive water transport processes which cannot be imaged by adding a contrast agent for exploiting the standard attenuation contrast imaging mode.

Introduction

The visualization of water transport processes in porous materials is relevant in several fields of natural and engineering sciences. An incomplete and limited list of examples would include water transport in polymer electrolyte membrane fuel cells during operation (Bazylak, 2009; Wang *et al.*, 2011), water drainage and evaporation in hydrogeology and soil physics and their relations with evolving climatic conditions (Or *et al.*, 2013) and a manifold of contaminated water transport mechanisms of interest in civil and environmental engineering (Wildenschild *et al.*, 2002; Dann *et al.*, 2011).

The list would also include water imbibition and drying in porous building materials, with associated degradation (Leemann & Loser, 2011) and shrinkage processes (Lura *et al.*, 2007), respectively, water redistribution in trees and plants (Lee & Kim, 2008) and the displacement of nonwetting liquid phases, e.g. oil or liquefied CO_2, by water in rocks, for the exploitation of hydrocarbons and for carbon capture and storage (Brown *et al.*, 2014; Andrew *et al.*, 2013).

In most cases, the transport process itself cannot be understood if the internal porous architecture is not studied simultaneously. Therefore, an increasing number of investigations have been dedicated to capturing the water transport features at length scales comparable with those of the pores (Wildenschild & Sheppard, 2013).

In this work, the focus is on drying of porous materials containing distilled water. We use drying as a case study for proposing and characterizing a specific approach to the pore-scale imaging of water transport in porous materials.

The spatio-temporal dynamics of a drying front in a porous material highly depends upon the pore space features (porosity, pore size distribution, pore space morphology and topology; Prat, 2002) and on pore scale processes, e.g. capillary forces-driven liquid transport (Scherer, 1990; Le Bray & Pratt, 1999; Xu *et al.*, 2008), in-pore evaporation and vapour diffusion (Lehmann *et al.*, 2008) and formation of liquid films on the pore surface (Yiotis *et al.*, 2003; Lehmann *et al.*, 2008).

Among the most used techniques for imaging water transport in porous materials we list neutron imaging, nuclear magnetic resonance and X-ray attenuation contrast imaging (XACI).

Neutron imaging allows achieving very high contrast between regions with different water content. The temporal resolution for a full tomography can be sufficient for investigating

Correspondence to: Michele Griffa, Center for X-ray Analytics and Concrete /Construction Chemistry Laboratory, Swiss Federal Laboratories for Materials Science and Technology (Empa), Überlandstrasse 129, CH-8600, Dübendorf (ZH), Switzerland. Tel: +41-58-765-4360; fax: +41-58-765-6935; e-mail: michele.griffa@empa.ch

water drying (Kaestner *et al.*, 2007) and also faster processes (Schaap *et al.*, 2008; Kaestner *et al.*, 2011) but a trade-off is inevitable with the spatial resolution, which, in standard setups, has not yet overcome the threshold of about 10 μm (see table 1 in Perfect *et al.*, 2014). Such spatial resolution threshold does not allow for imaging a large fraction of the pore space in most porous materials. Another limitation of neutron imaging consists in the small number of facilities where it can be performed and their respective temporally limited access.

Nuclear magnetic resonance methods are very useful for the simultaneous spatial mapping of water content (by magnetic resonance imaging) and spatially resolved pore size distribution estimation (by nuclear magnetic resonance relaxometry) during drying (Choi *et al.*, 2000; Valckenborg *et al.*, 2001; Faure *et al.*, 2012). Magnetic resonance imaging achieves as well very high sensitivity to small changes in local water content. The spatial resolution strongly depends upon the range of the applied magnetic field gradient and upon the presence of magnetic impurities in the materials. As a result, direct imaging of the micron scale pores may not be feasible with conventional instruments (Pel & Huinink, 2012). In terms of temporal resolution, nuclear magnetic resonance methods are more limited than neutron imaging, still they can be used to investigate both slow processes as drying and faster ones as capillary imbibition (Mitchell *et al.*, 2013).

Standard X-ray imaging, at the laboratory scale or with synchrotron radiation, has been extensively and successfully used for investigating water transport in porous materials, including drying (Shokri *et al.*, 2009; Shokri & Sahimi, 2012). Contrary to neutron and magnetic resonance imaging, high spatial (hundreds of nanometers; Stampanoni *et al.*, 2010) and temporal (a few seconds with synchrotron radiation; Berg *et al.*, 2013; Mokso *et al.*, 2013; Youssef *et al.*, 2013; half-minute or slightly less with laboratory sources; Myers *et al.*, 2011; Bultreys *et al.*, 2015) resolutions are nowadays achievable by many tomography instruments/facilities, making it possible to systematically and extensively investigate pore-scale mechanisms (Wildenschild & Sheppard, 2013).

Standard X-ray imaging is mainly based upon the attenuation of the X-ray beam transmitted through the object. Typically, photon photoelectric absorption and Compton scattering are considered as the main interaction processes responsible for the X-ray beam overall attenuation, up to an energy of 1 MeV (Attix, 1986; Banhart, 2008). In this view, other processes as diffuse scattering or X-ray refraction are neglected, even though, physically, they are always present.

The contrast in the images due to X-ray attenuation is typically described as based upon the spatial distribution of β, the imaginary part of the complex index of refraction n, usually written for the X-ray energies as $n = 1 - \delta + i \cdot \beta$. β is proportional to Z^n, with $n \cong 4 - 5$, and to E^{-m}, with $m \cong 3 - 3.5$, Z being the atomic number of the element and E the photon energy (Banhart, 2008). We term standard X-ray imaging as XACI.

XACI of water transport in porous materials is typically performed in the hard X-ray range ($E \geq 5$ keV). Lower energies are typically not suitable to achieve sufficient signal-to-noise levels in photon detection within reasonable measurement times. Furthermore, because of representative element volume constraints, it is not possible to reduce arbitrarily the size of such heterogeneous samples as porous materials, to try to increase the X-ray transmission at lower energies.

With XACI, spatio-temporal changes in pore-scale water content can be resolved only when the pores are at the hundreds of μm – mm scale and/or the transport process leads to a large change in the saturation degree (fraction of pore volume filled in by water), e.g. from complete saturation to empty pores (Ketcham & Iturrino, 2005; Kohout *et al.*, 2006; Sant & Weiss, 2009; Pease *et al.*, 2012; Wang *et al.*, 2012). For porous materials with pore size distribution extending into the μm and sub-μm ranges, as in the case studied in this work, it may be unfeasible to resolve the local water content changes, due to (1) the small X-ray attenuation by water compared with the one by the porous substrate and (2) the small water volume changes at the pore-scale.

In the latter case, the most frequently adopted work-around consists in using a water-based salt solution, containing elements with high Z, instead of distilled water. For example, concerning visualization of drying in porous media, water-based solutions of CaI (Shokri *et al.*, 2009; Shokri & Sahimi, 2012) and a suspension of limestone powder in water (Prime *et al.*, 2015) have been used. Salt precipitation during drying of porous media has been successfully imaged with XACI for NaCl solutions (Norouzi Rad *et al.*, 2013; Norouzi Rad & Shokri, 2014). Concerning other water (and more generally liquid) transport processes, pore-scale, multiphase (wetting and nonwetting) fluid displacement/interfacial mechanisms have been investigated by XACI using CsCl (Berg *et al.*, 2013; Armstrong *et al.*, 2014a, b; Brown *et al.*, 2014) and KI (Youssef *et al.*, 2013; Andrew *et al.*, 2013, 2014) solutions. In those studies, the solution contributed also to increase the difference in X-ray attenuation between the wetting phase (the water-based solution) and the nonwetting one (e.g. oil). XACI plus a CsCl solution (Boone *et al.*, 2014) or a mixture of diiodomethane and toluene (Ghous *et al.*, 2007) have been used to identify the spatial distribution of pores with size below the spatial resolution in rocks.

When the target of investigation is a water transport process, the use of water-based salt solutions to increase the X-ray attenuation of the liquid implies a careful and complicated choice of the salt and of its concentration in order to reduce as much as possible the mismatch between pure water and the solution interfacial, e.g. surface tension and contact angle, and transport, e.g. density and viscosity, properties (Franzoni *et al.*, 2014). This represents a strong limitation in using XACI in combination with water-mimicking liquids leading to enhanced X-ray attenuation. An additional limitation consists in the increase of beam hardening artefacts,

as thoroughly documented by Nakashima & Nakano (2012), Nakashima (2013) and Nakashima & Nakano (2014).

Finally, the use of solutions instead of distilled water for XACI is not feasible in the case of chemically reactive transport processes, e.g. most of water transport processes in cement-based materials, due to cement hydration reactions, and water transport in polymer electrolyte membrane fuel cells under operation conditions.

In order to visualize water transport processes for porous materials with pore size distribution extending in the μm and sub-μm range and/or for partial pore-scale saturation/desaturation, other X-ray imaging approaches should be adopted. Potentially useful alternative methods are those based upon the direct or indirect spatial mapping of the decrement of the real part of the index of refraction, δ.

X-ray dark-field contrast imaging exploits the reduction in spatial coherence of the X-ray beam transmitted through the sample due to the heterogeneity of δ's spatial distribution at a length scale smaller than the imaging system spatial resolution. Such heterogeneity leads to multiple refraction (scattering) of the X-ray photons, breaking up the spatial coherence of the inspecting beam. Yang *et al.* have shown that water displacements in a porous material with pore size distribution covering a range falling below the spatial resolution lead to a decrease in the local multiple scattering, thus enhancing the contrast between regions of the material with empty pores and regions with partial or complete saturation (Yang *et al.*, 2014). The proof-of-concept of that approach was implemented via Talbot–Lau interferometry (Yang *et al.*, 2014). Another possible implementation of that approach could be based upon the edge illumination technique (Endrizzi *et al.*, 2014). With either technique for performing X-ray dark-field contrast imaging, the main limitation with the current technology/methodology lies in the small temporal resolution for performing tomography.

X-ray phase contrast imaging (XPCI) promises to have a very high success potential. It is based upon the retrieval of the contributions by X-ray refraction to the transmitted photon intensity distribution. It consists in the qualitative or quantitative (phase imaging) mapping of the spatial distribution of δ at a length scale larger than the spatial resolution. Several possible implementations for XPCI exist, namely, Talbot–Lau interferometry (Clauser & Reinsch, 1992; Momose, 1995; Weitkamp *et al.*, 2005; Pfeiffer *et al.*, 2006), edge illumination (Olivo & Speller, 2007; Olivo *et al.*, 2009; Munro *et al.*, 2012), crystal analyzer-based imaging (Chapman *et al.*, 1997; Bravin, 2003), crystal interferometry (Bonse & Hart, 1965; Momose *et al.*, 1996) and free-space propagation (FSP) (Nugent *et al.*, 1996; Cloetens *et al.*, 1997; Gureyev *et al.*, 2009). The last technique is the most promising for the targets of this work because it allows achieving very high temporal and spatial resolutions, especially when implemented at synchrotron radiation beamlines. At the same time, it allows achieving high contrast to the local, spatio-temporal variations in the distribution of material phases made up of low Z elements (Mokso *et al.*, 2013). These features imply the potential of simultaneously imaging the porous substrate and the water transport process. Finally, FSP-XPCI has higher sensitivity to partial changes in pore-scale water content compared with XACI (see section S1 of Yang *et al.*, 2015, for a physical explanation and respective quantitative examples).

The potential of FSP-XPCI of pure water in natural and engineering materials was already hinted at by Mayo (2012), as well as Wildenschild & Sheppard (2013). Derluyn *et al.* showed that a Na_2SO_4 solution and respective crystals, precipitated within a limestone pores due to either wetting/drying cycles or cooling, could be identified with FSP-XPCI and not with XACI (Derluyn *et al.*, 2014).

In this paper, we systematically show the potential and advantages of FSP-XPCI in visualizing pure water transport processes in porous materials. We performed both XACI and FSP-XPCI of the same exact sample of a natural porous material (Globigerina limestone), at two different stages of water drying, in the absence of any contrast agent. By 3D image analysis of the time-differential tomogram (described in the section 'Materials and methods'), we show the advantages of XPCI over XACI and that pore-scale features of the drying process can be identified and quantitatively analysed (section 'Results'). In section 'Discussion, outlook and conclusions', we build upon the results to draw conclusions about what can be gained by the combined use of tomographic XPCI and 3D image analysis in terms of a better understanding of pure water drying in porous materials and which are the possible gains for pore-scale investigations of other water transport processes.

Materials and methods

Materials, sample preparation and measurement protocols

Globigerina limestone is a soft and highly porous (up to 41% in total open porosity, see Franzoni *et al.*, 2014) limestone coming from Malta. It has been used as a building material for about 6000 years (Cassar, 2002). It is frequently adopted as a model system to investigate environmental weathering of building stones (Franzoni *et al.*, 2013). From a chemical point of view, it is composed of carbonates (about 90% by mass), by small amounts of quartz (8%) and by some clay traces (12%) (Franzoni *et al.*, 2014). The high content in carbonates is due to $CaCO_3$ crystals, calcareous cementitious layers and different types of fossils, e.g. shells, algae and planktonic fossils, for example, foraminifera Globigerina. Its large open porosity, compared with other limestones, is due to a large fraction of coarse pores (average pore radius from 2 to 3 μm, measured by mercury intrusion porosimetry, MIP, by Franzoni *et al.*, 2013, 2014).

We used a Globigerina limestone cylinder 35 mm high and about 4.5 mm in diameter, cored while being flushed with water from a larger sample (a cuboid with lateral size of about

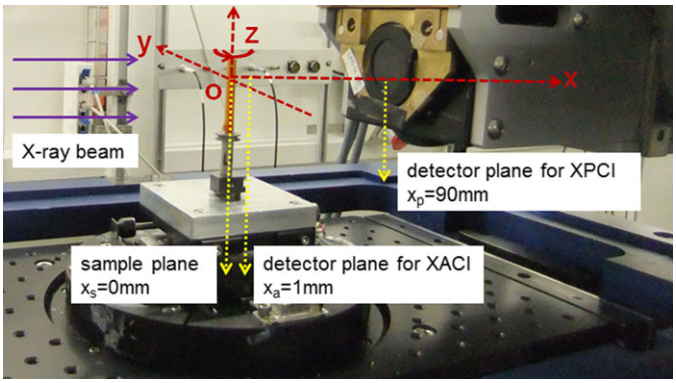

Fig. 1. Representative picture of the sample mounted on the stage of the TOMCAT X-ray tomographic microscope with indication of the coordinate system and the detector positions for attenuation and phase contrast imaging measurements, respectively.

50 mm). After 4 days of oven drying at 50°C, the sample was glued on a metallic sample holder.

The drying + imaging experiments consisted in performing X-ray tomographic microscopy (XTM) with synchrotron radiation, at two water saturation stages (high saturation degree and after drying for a given time Δt_{drying}). The high level of saturation was achieved by submerging the sample into distilled water for about 1 h at low vacuum (about 5 mbar), in order to remove as much as possible air bubbles from the pore space. After water saturation the lateral surface of the sample was covered with a 70 μm thick polyimide film, except for the top surface, in order to constrain the evaporative drying mainly along the symmetry axis of the sample and make only one lateral surface (top) available for evaporation. Polyimide is a material with a high degree of X-ray transparency. The sample was then kept immersed in de-ionized water at room conditions till the first set of XTM measurements, after which it was moved into a container with internal relative humidity (RH) of the order of 1–5%, flushed with N_2 gas, to accelerate drying as much as possible. After about $\Delta t_{\text{drying}} = 2.5$ h we performed the second set of XTM measurements.

X-ray tomographic microscopy

According to the transport of intensity equation, the transmitted X-ray intensity distribution on the detection plane is related only to the linear projection (also called Radon transform) of β, P_β, when the detection plane coincides with the exit plane of the object (Paganin, 2006). When the detection plane is far away from the sample's exit plane, the transmitted intensity distribution encodes information about both P_β and the second-order partial derivatives of P_δ calculated on the detection plane (Paganin, 2006).

We performed XTM at the TOMCAT beamline of the Swiss Light Source, at the Paul Scherrer Institute. At each saturation stage (before and after drying), we performed six XTM scans. Figure 1 shows an example of sample mounting, the measurement configuration and the coordinate system.

Three scans were performed with the detector as close as possible to the sample (about 1 mm distance along the *X*-axis) and differed for the region of interest (ROI) scanned. These scans were used for XACI. The three ROIs were adjacent to each other along the Z-axis, starting from the top evaporation surface. The same three ROIs were then scanned again but positioning the detector at 90 mm from the sample along the *X*-axis. These other scans were used for XPCI.

At the TOMCAT beamline the X-ray source is a superbend magnet (2.9 T) followed downstream by a multilayer monochromator, by which the X-ray beam energy in our study was tuned to $E = 30$ keV ($\lambda \sim 0.04$ nm) with a bandwidth $\Delta E/E$ of 2%. The choice of this X-ray energy resulted from optimization of the raw radiograph signal-to-noise ratio and temporal resolution.

The detection system consisted in a 300 μm thick Ce-doped LAG scintillator, converting the X-ray photons into visible light photons, then conveyed onto a pco.edge 5.5$^{\text{TM}}$ sCMOS detector by lenses with optical magnification factor $M \cong 2.96$. The sCMOS detector has physical pixel size $p = 6.5$ μm and 2560×2160 pixels in the *Y*- and Z-directions, respectively. Taking M into account, the field of view (FOV) was 5.621 mm in *Y*- and 4.743 mm in Z-directions, respectively, with effective pixel size $p_e = 2.196$ μm. The actual FOV was restricted to 1520 pixels in the Z-direction, corresponding to about 3.338 mm. Such restriction was due to the choice of the operating beam energy (the Z-size of the beam is energy dependent). The exposure time for the detector was 50 ms for each radiograph. Each XTM scan consisted of 1501 radiographs of the sample at different orientation angle θ (rotation angle around the Z-axis) in respect to the detection plane, with θ between 0° and 180°. In addition, for each scan, we acquired 10 radiographs in the absence of the beam (dark fields) and 100 radiographs in the absence of the sample (flat fields), to correct the radiographs for the illumination beam spatial inhomogeneity and any pixel-wise offset signal.

The overall time for each single scan was about 9 min, considering 100 ms detector stabilization time for each radiograph and the sample rotation time.

Tomographic reconstruction and datasets

For each saturation stage and each ROI, we performed the XACI datasets tomographic reconstruction assuming the Beer–Lambert law describing the relationship between the radiographs' pixel values and the linear projection of β, P_β.

The reconstruction of the spatial distribution of β inside the sample from the set of radiographs at different θ's, was performed with the Gridrec algorithm as implemented at the TOMCAT beamline (Marone & Stampanoni, 2012).

For each saturation stage and each ROI, the first XPCI processing step consisted in the phase retrieval, i.e. calculating the linear projection of δ, P_δ, as a function of the detector pixel values. We chose the phase retrieval equation proposed by Paganin *et al.*, based upon the transport of intensity equation and some restrictive assumptions (Paganin *et al.*, 2002). The assumptions are (1) the sample is made of material phases having the same ratio $\frac{\delta}{\beta}$, being it a known parameter, and (2) the detector must be located in the near-field (Fresnel diffraction) region along the beam path. Assumption (2) is a direct necessity for using a formalism based upon the transport of intensity equation and was satisfied in our case by choosing the sample-to-detector distance $d_{sd} = 90$ mm. Assuming a level-of-detail l to be resolved in the reconstructed XPCI images equal to two times p_e ($l \cong 4.4$ μm), at the chosen beam energy the Fresnel number $N_F \equiv \frac{l^2}{\lambda d_{sd}} \cong 5 > 1$ (value delimiting the Fresnel diffraction region). Assumption (1) is not respected by the type of sample due to the presence of two material phases (other than air) with different $\frac{\delta}{\beta}$ values, water and (mainly) $CaCO_3$. However, the degree of violation of that assumption is limited by the high degree of chemical and spatial homogeneity of the porous substrate (local changes in mass density for the limestone do not affect the spatial distribution of $\frac{\delta}{\beta}$).

Despite the fact that the Paganin *et al.* (2002) algorithm can be used mainly for qualitative phase contrast imaging in the case of nonpure phase objects, it has the advantage of being very robust in terms of a reduced number of artefacts when applied to case studies not satisfying completely its two basic assumptions, especially the constant $\frac{\delta}{\beta}$ one (Beltran *et al.*, 2010; Weitkamp *et al.*, 2011; Boone *et al.*, 2012; Irvine *et al.*, 2014).

Since the sample is not made of material phases with equal $\frac{\delta}{\beta}$ values, the δ ($= 6.3 \times 10^{-7}$) and β ($= 7.5 \times 10^{-10}$) values were chosen by a coarse, direct exploration of the $(\delta; \beta)$ space, having as starting point the theoretical values for $CaCO_3$ calculated at the given beam energy E by using the LBNL CXRO database of photon interaction cross-sections (Henke *et al.*, 1993), and searching for a point maximizing the images' signal-to-noise ratio (see the section 'Results', Eq. (1), for its definition) for pore regions and contrast-to-noise ratio (see Section 'Results', Eq. (2)) between voxel values of pores and the solid limestone skeleton. The procedure followed for evaluating such signal-to-noise and contrast-to-noise ratios for those material phases was similar as the one reported in the 'Results' section, used to compare XACI and XPCI images. The phase retrieval in correspondence of each $(\delta; \beta)$ was performed by using the implementation of Weitkamp *et al.* (2011), of the Paganin *et al.* algorithm.

After phase retrieval, tomographic reconstruction of the δ spatial distribution was performed with the same Gridrec algorithm.

Tomographic datasets: processing and analysis

In what follows '3D image' will be used with the same meaning of 'tomographic dataset'.

The main goals of the 3D image analysis were (1) the 3D visualization of pores with equivalent diameter larger than the spatial resolution (about 9–10 μm, due to voxel rebinning, see below) and (2) mapping the spatial redistribution of water as a consequence of the drying process. Related with point (2), we focused only on identifying (segmenting) regions affected by water loss during the evolution between the two saturation stages, since that is one of the major pore-scale effects of drying.

We restricted the analysis, for both the XACI and XPCI images and for both saturation stages, to the first top ROI. We thus analysed four 3D images.

We performed mutual 3D image registration (alignment) of the four images assuming as deformation model only a rigid body (translation + rotation) one. The registration was performed with software in ImageJ/Fiji (Schindelin *et al.*, 2012). After alignment, we selected only the top 900 (out of the 1520) digital cross-sections composing the 3D images and orthogonal to the Z-axis of the sample. Such cross-sections will be termed 'slices' from now on.

We cropped each slice to a size of 2280×2280 pixels. We then applied a $2 \times 2 \times 2$ voxel rebinning. The cropping and rebinning was needed to reduce the computing time and RAM memory required for each analysis step. The actual size of the analysed 3D images was then $1140 \times 1140 \times 450$ (X, Y, Z directions, respectively) and the bit depth was 32.

In order to automatically exclude from any voxel-based calculation the region surrounding the sample in each image, we segmented that region by a constrained region growing algorithm implemented in the Empa Bundle of ImageJ Plugins for Image Analysis, EBIPIA (plugin 'Segment Phases 3D') (Münch, 2014) and created a 3D binary (8-bit) image identifying it. The region surrounding the sample will be called in the following R.

We achieved goal number (1) (pore segmentation) using both XACI 3D images in combination with R, i.e. considering for each image only voxels not belonging to R. Considering those voxels of the two XACI images as statistical ensembles

of voxels, we applied to each of them a *K*-means clustering algorithm (MacQueen, 1967; Jain *et al.*, 1999) with 1D feature space consisting in the voxel value axis only, i.e. characterizing each voxel only by its value. The algorithm is implemented as well in the EBIPIA (plugin 'Cluster image' based upon the approach by Kanungo *et al.*, 2002). We searched for $K = 3$ clusters, corresponding to three sets of voxels (material phases): pore voxels, low density $CaCO_3$ voxels and high density $CaCO_3$ ones. At the end of the algorithm's iterations, we chose the cluster with lower average voxel value as the one corresponding to the subset of pore voxels. This procedure led to a new voxel subset for each XACI image.

We created then a 3D binary image as a mask identifying the pore voxels. Figure S3 in Yang *et al.* (2015), shows such mask.

The choice of XACI 3D images for the pore voxel segmentation was motivated by their availability in our case and by their higher spatial frequency content compared with XPCI ones (Irvine *et al.*, 2014).

Any quantitative analysis of the pore space, based upon the segmented pores, should thus be more precise if performed on segmentation results from XACI datasets.

We addressed goal (2) by using the XPCI images in association with the mask *R*, i.e. considering only voxels inside the sample volume, as done for the XACI images. We calculated then a new 3D image obtained as the voxel-wise difference between the XPCI image before drying and the one after drying. Voxels in such time-differential image belonging to *R* were assigned a constant equal value. Classification into different subsets of the time-differential voxel values for the pore voxels was performed by best fit of the time-differential voxel value histogram with a Gaussian mixture model and by choosing as thresholds the best fit estimates of the Gaussian averages $\pm$ the respective standard deviations. We performed the histogram best fit with the expectation maximization (EM) method (Dempster *et al.* 1977) implemented in Matlab by Roughan (2009).

Finally, we analysed the pore size cumulative distribution (PScD), in order to establish correlations between the water loss regions, the pores and their geometrical features. For such purpose, we performed on the pore binary image a 'continuous' PScD analysis (Torquato, 2002; Ye, 2003; Münch & Holzer, 2008), implemented according to the algorithm of Münch & Holzer (2008), in the plugin 'Pore size distribution' of the EBIPIA (Münch, 2014). This method allows achieving (1) PScD curves from binary images of segmented pore systems which can be compared with experimental MIP ones, since relying on an analogous definition of PScD, and (2) a physically meaningful PScD estimate for pore systems characterized by a high degree of interconnectivity, for which 'discrete' PScD estimates based upon calculation of individual pore equivalent sphere radius are not meaningful since the pores are not actually separated distinct objects with spheroidal shape. Moreover the 'discrete' PScD definition is not even geometrically comparable with a MIP process (Münch & Lorenz, 2008).

To compare the cumulative PScD obtained from the image analysis with experimental data we performed 2-cycle MIP measurements with a Pascal 440™ (Thermo Fischer Scientific Inc.) porosimeter on additional crushed samples from the same batch of the tomographed sample. Finally, we also measured the total open porosity on five independent samples, still from the same batch, by gravimetric measurements and water submersion under low vacuum conditions (5 mbar).

The 'continuous' PScD definition of Münch and Holzer and the respective code implemented in EBIPIA also allows producing a 3D spatial map of 'pore size' (also called 'pore radius') by associating to each voxel belonging to the pore binary image a value corresponding to the maximum radius of a sphere containing that voxel and still fitting inside the pore system. Exploiting this feature, we could calculate for each disconnected region of the pore binary image, i.e. for each pore, the average pore radius, *r* (average of all the voxel pore radius values) and its degree of desaturation, *DS*, defined as the ratio between the total number of its voxels classified as water loss voxels (in-pore water loss volume, as obtained from the pore segmentation) and its total number of voxels (pore volume). The curve *DS* versus *r* is used to assess whether the water loss spatial distribution is physically meaningful from the point of view of the pore-scale drying process, thus assessing the usefulness of pore-scale XPCI of water drying.

Results

Comparison of attenuation and phase contrast images, before and after drying

The visual inspection and qualitative analysis of the raw 3D images did not allow a complete identification of water loss regions (goal number 1).

Figures 2(A) and (B) show two slices taken at the same position from the XPCI images before and after drying, respectively. Figures 2(C) and (D) show corresponding slices taken from the XACI images.

Each slice, for each image type, was actually taken from the respective image after some preprocessing used only with the purpose of allowing for a fair visual comparison between the images at the two drying stages (see section S2 of Yang *et al.*, 2015, for the details).

The visual comparison between Figures 2(A, B) and (C, D), respectively, shows that a slight decrease in the average voxel value is observable in the XPCI images, from Figures 2(A) to (B), although less can be perceived in the XACI images, from Figures 2(C) to (D). A decrease in voxel value is expected for both datasets because drying leads mainly to water loss, thus a voxel-wise decrease both in β and δ. Such drying effect can be better appreciated by looking at the inset in each column of

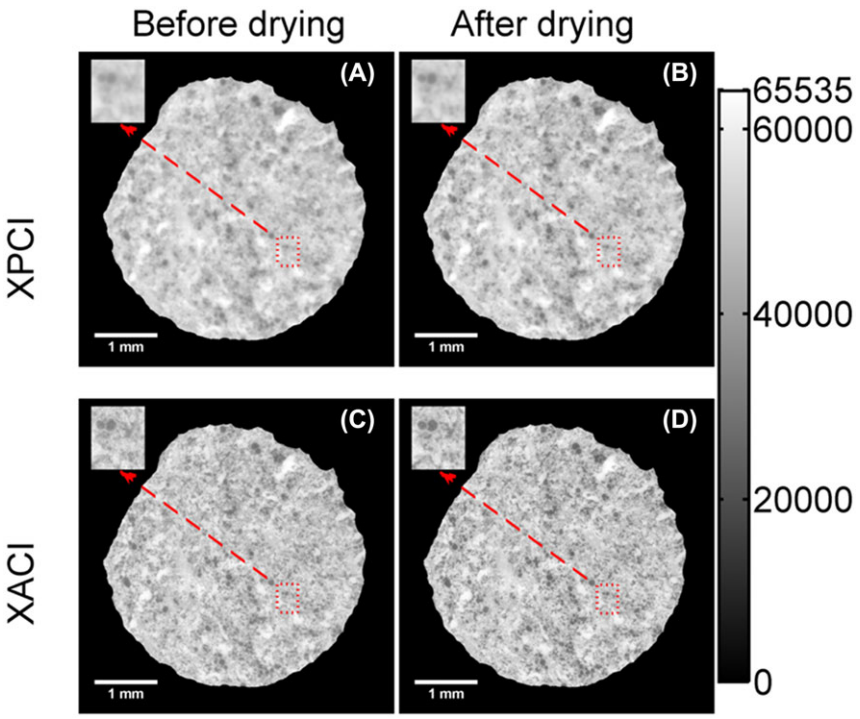

Fig. 2. *X–Y* cross-section (slice) from the X-ray phase (A and B) and attenuation (C and D) contrast tomographic datasets, respectively, all taken at the same position. Blocks (A) and (B) refer to the water saturated stage, whereas (B) and (D) after drying, respectively. The top-left inset in each block is a zoom into a small ROI indicated by the dashed rectangle. Each 3D image of a given type was rescaled to a common dynamic range according to the procedure described in section S2 of Yang *et al.* (2015), for visual comparison only. Voxels belonging to the region surrounding the sample were automatically assigned the same value equal to 0. Pores are darker in each image type, while the limestone is brighter. Very bright regions in the porous substrate correspond to either higher density $CaCO_3$ regions or regions with quartz or clay inclusions.

Figure 2, highlighting the same small ROI for each dataset. In the XPCI slices (Fig. 2A and B) drying contributed to decreasing the level of blurring, especially inside the pores and at their boundaries with the solid matrix. In the XACI slices (Fig. 2C and D) no significant change is noticed.

We also observe that in general, at any drying stage, the XPCI slices are more blurred than the XACI ones, due to the fact that phase retrieval algorithms usually act as low pass (spatial) frequency filters (Irvine *et al.*, 2014). Thus, the spatial resolution is expected to be better in the XACI images. This is the reason why they were chosen for segmenting the pores (fig. S3 in Yang *et al.*, 2015). However, the XPCI images exhibit larger contrast between different material phases and, of particular interest in this work, between pores and solid matrix.

We characterized such differences between the two types of images by calculating the signal-to-noise and contrast-to-noise ratios, SNR_i and CNR_{i-j}, respectively, for different material phases i and j. The parameters are defined as

$$SNR_i = |S_i|/\sigma_i\,, \tag{1}$$

$$CNR_{i-j} = \left|S_i - S_j\right|/\sqrt{\sigma_i^2 + \sigma_j^2}, \tag{2}$$

Table 1. Signal-to-noise ratio (SNR) of pore, solid limestone and air regions and contrast-to-noise ratio (CNR) between pore and solid regions, calculated via Eqs. (1) and (2). The values are calculated over several ROIs defined on slices (the first one every 50). The ROIs were equal for each type of dataset and at each drying stage.

Dataset (3D image)	SNR_{pore}	SNR_{solid}	SNR_{air}	$CNR_{pore\text{-}solid}$
XPCI, before drying	11.69	17.36	0.85	11.50
XPCI, after drying	9.46	17.45	0.93	9.32
XACI, before drying	8.75	12.67	0.14	7.76
XACI, after drying	7.75	12.50	0.11	6.88

where S_i and σ_i are the average and standard deviation of the voxel value over a set of ROIs covered by the material phase i. The material phases we considered are (1) air outside the sample, (2) pores (filled in with air and/or water) and (3) the solid material of the limestone. The two parameters of Eqs. (1) and (2) were calculated from a set of ROIs defined on the first of every 50 slices from the 3D images. For a given slice, the ROIs were chosen identical for each image. Table 1 reports the results of such analysis. The XPCI images exhibit larger *SNR* compared with the XACI ones, for all the three

material phases considered, in agreement with the higher level of blurring visible in Figure 2(A). This difference may simply be due to the above cited low-pass filter nature of the type of phase retrieval used and may not bring any advantage for distinguishing between filled and empty pores.

We also notice that the *SNR* for the pore only ROIs undergoes in both image types a drop in correspondence of drying, due to an increase in physical properties mismatch between the pore and the stone matrix, which leads to stronger microscopic photon scattering. Since the image formation models XPCI is based on are more sensitive to the macroscopic effects of such microscopic scattering. although the models XACI is based on are less, in correspondence of the water content change the *SNR* drop is larger in the XPCI images than in the XACI ones (19% vs. 11%, respectively). This indicates that XPCI images undergo larger changes due to water content changes than the XACI ones.

The *CNR* between pores and the limestone substrate (the two material phases of interest from the point of view of pore-scale water visualization) is larger in the XPCI images as well, indicating a better distinction between pores and the solid phase of the porous medium.

Despite the larger *CNR* between pores and solids and larger changes due to drying in the XPCI images compared with the XACI ones, none of them could be used alone for a reliable and absolute identification of water loss regions. This fact is additionally documented by figures S4 and S6 in Yang *et al.* (2015), which report the cumulative distribution functions (CDFs) of the voxel values for the four images shown in Figure 2. Those CDFs better show the slight decrease in voxel value for the XPCI images while a smaller decrease for the XACI ones is observed. Still the difference is very small even for the XPCI images. In addition, the CDFs indicate that the voxel value distribution function is, for both image types and at any drying stage, a univariate Gaussian function (see also figs. S5 and S7 in Yang *et al.*, 2015). Thus, segmentation of water regions (voxels) from any raw 3D image, of any type and at any drying stage, was not feasible.

Time-differential phase contrast imaging results

Figure 3 shows the slice taken at the same position as that of Figure 2 but from the time-differential XPCI (inset (A)) and XACI (inset (B)) images. For any contrast type, the time-differential image was calculated as the voxel-wise subtraction between the image before drying and the image after. Such images were already corrected for the different offsets but not rescaled to the integer value interval [0; 65535] before the subtraction was performed. After subtraction, each time-differential image was then rescaled such that the minimum/maximum voxel value range of pore voxels was remapped to the integer interval [0; 65535]. Voxels belonging to the out-of-sample region R were assigned value 0.

Brighter voxels in Figure 3(A) or (B) indicates a local, larger decrease in δ and β, respectively, which can be due to water loss during drying. Darker voxels can indicate either no change or a small increase in δ and β, respectively. An increase may be due to local water gain produced by water displacements driven by capillary forces (Lehmann *et al.*, 2008; Xu *et al.*, 2008). The visual comparison of Figures 3(A) and (B) is already sufficient to highlight the large difference between the XPCI and XACI time-differential images. Very well defined regions characterized by a decrease in voxel value appear clearly in the XPCI time-differential image, with strong voxel value contrast to the surrounding regions, although such high contrast is not achieved in the XACI time-differential image, where the voxel value is more homogeneously distributed, thus the image is noisier. This result is expected, as mentioned in section S1 of Yang *et al.* (2015), if one considers water redistribution and what it brings to a voxel value in the two types of images. At 30 keV, the relative difference in β between water and $CaCO_3$, $(\beta_{CaCO3} - \beta_{water})/\beta_{water}$, has value 29.676, whereas the corresponding relative difference for δ, $(\delta_{CaCO3} - \delta_{water})/\delta_{water}$, is 1.435. See also figure S2 in Yang *et al.* (2015). This means that a volume of water moving from a source voxel to a destination one or simply disappearing in a voxel because of evaporation results in a larger voxel value change and contrast enhancement between a water-filled pore and the solid matrix for the image based upon δ than for the one based upon β. As a consequence, the time-differential XPCI image of Figure 3(A) allows for an unambiguous and direct visualization of pore-scale water loss regions while the time-differential XACI image does not.

A quantitative confirmation of the difference between the two types of time-differential images comes from the value histograms for the pore voxels. Figure 4 shows such histograms for the time-differential images after the 16 bit unsigned integer encoding. For the XPCI time-differential 3D images, a multimodal voxel value distribution clearly appears (Fig. 4A), suggesting the possibility of identifying different types of voxels, although the XACI time-differential image is characterized by a unimodal, Gaussian-like distribution (Fig. 4B), indicating just a noise-like distribution.

Segmentation of water content change regions

We sorted out the pore voxels into different subpopulations based upon the histogram in Figure 4(A), assuming each subpopulation to be Gaussian-like distributed. Figure 5 shows the results of the Gaussian mixture best fit based upon the assumption of three subpopulations and the EM method. The Gaussian distribution of each subpopulation is plotted along with their sums and the data from Figure 4(A). The best fit was better with three subpopulations than just with two (see section S5 in Yang *et al.*, 2015 for the comparison of the two best fits). The subpopulations with the lowest and the highest average values can be interpreted as containing water gain and water

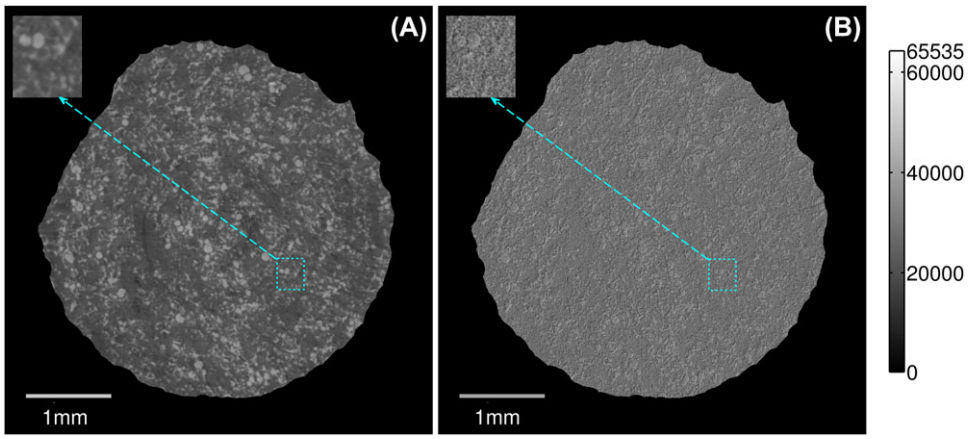

Fig. 3. Time-differential phase (A) and attenuation (B) contrast 3D images, obtained by voxel-wise subtraction of the image after drying from the image before drying. For each contrast type, the voxel value range was remapped from its minimum/maximum range inside the pore 3D binary image to the integer value interval [0; 65535], assigning value 0 to any voxel belonging to the out-of-sample region. The top-left insets in each column show a zoom into the same ROI as for Figure 2. Brighter voxel values correspond to a decrease in δ and β, respectively, for (A) and (B), while darker to either no change or an increase.

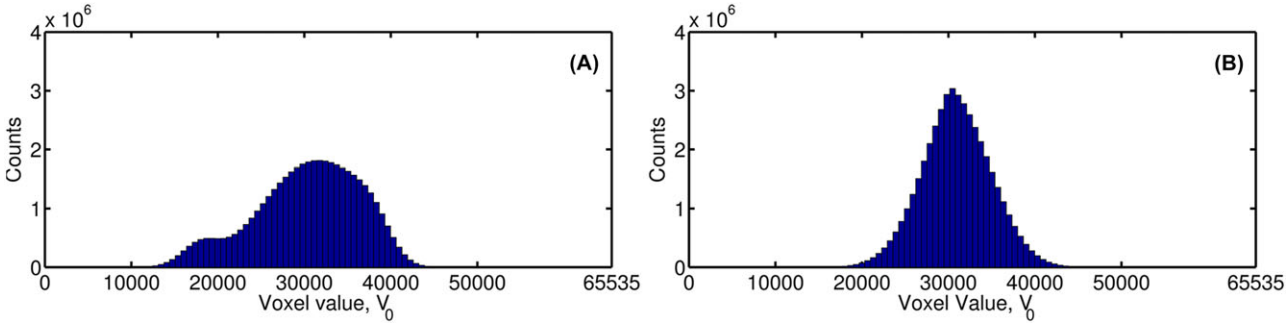

Fig. 4. Histograms for the values of the voxels belonging to the pore binary image, segmented from the attenuation contrast images, for the time-differential phase (A) and attenuation contrast 3D images, respectively.

loss pore voxels, respectively. The subpopulation with intermediate average value can be thought of as including voxels with either no change in water content or partial change or initial partial saturation degree (pores not completely filled up at the time of the first set of measurements).

As criterion to identify only the pore voxels characterized by a complete or partial water loss, we chose to fix a voxel value threshold $\tilde{V}_0$defined as the average value of the intermediate subpopulation *minus* its standard deviation (vertical dashed line in Fig. 5) and to consider only voxels with value above that threshold. This choice may lead to overestimate the amount of pore volume characterized by water loss. However, as seen in Figure 5, it allows for a clear distinction between the pore voxels with predominant water gain and those with partial or complete water loss, since the threshold falls approximately in the middle between the two Gaussian functions with the lowest and the largest average value, respectively.

Figure 6(A) provides an example of which pore voxels have been identified as water loss voxels. A slice, at the same position, is taken from three different 3D images, the XACI image after drying, the pore binary image and the 3D binary image containing the segmented water loss voxels. We chose the XACI image after drying to show the sample microstructure because the spatial resolution is supposed to be higher for that image than for any other, given the lower spatial resolution of the XPCI datasets and a slightly larger blurring due to water saturation in the XACI image before drying than after. It can be seen that most, but not all, of the segmented pores underwent water loss, suggesting that drying, up to the stage of the second measurements, did not empty completely all the pores or, alternatively, some pores were not filled in with water already before drying or some pores got refilled with water.

Water loss appears to have occurred rather isotropically, with no specific localization or preferential orientation, both on the slice plane and in 3D (see Fig. 6B for volumetric rendering of a corresponding 3D ROI including the slice in Fig. 6A and fig. S11 of Yang *et al.*, 2015, for a vertical slice). Once water loss regions inside pores are segmented by exploiting the time-differential XPCI image, it is possible to expand the comparative analysis of XPCI and XACI images in terms of

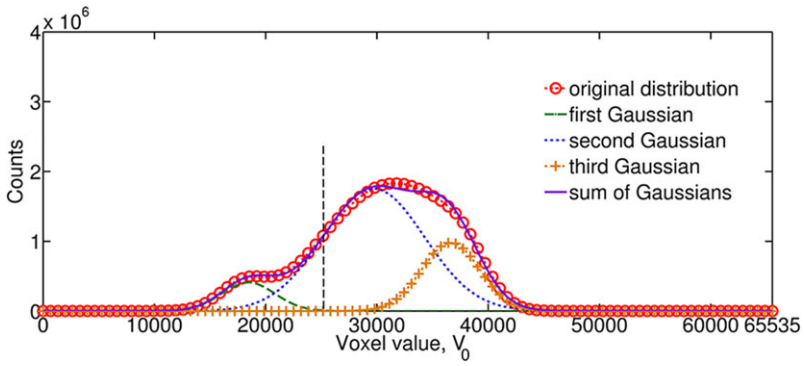

Fig. 5. (colour in the online version). Gaussian mixture best fit of the voxel value histogram (open circles) for the time-differential phase contrast 3D image, excluding the out-of-sample voxels and considering only pore voxels. A 3-Gaussian model allowed achieving the best fit of the original histogram. Each Gaussian distribution (dashed, dotted and dot-crossed lines) is plotted as well as their sum (solid line). The vertical dashed line represents the voxel value threshold $\tilde{V}_0$ to sort out pore voxels characterized by partial or complete water loss (voxels with value $V_0 \geq \tilde{V}_0$). $\tilde{V}_0$ was calculated as the average value of the center Gaussian (dotted line) *minus* its standard deviation.

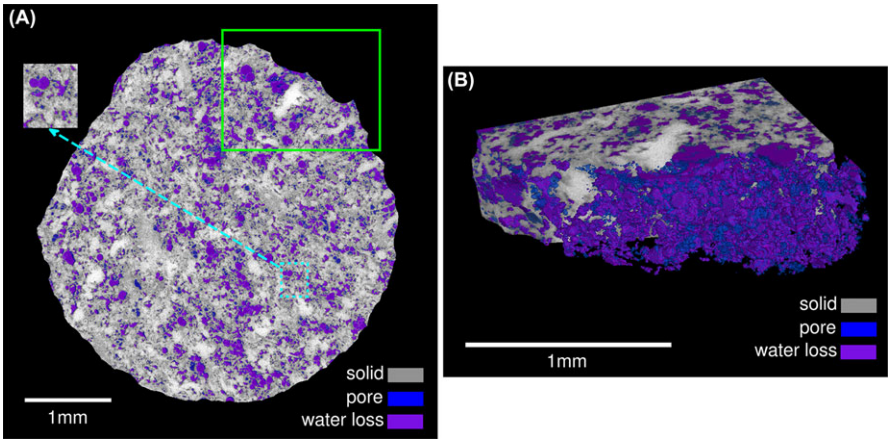

Fig. 6. (colour in the online version). (A) Slice from the attenuation contrast 3D image after drying, taken at the same position of the slices in Figures 2(C) and 3(B), with the segmented pore and water loss voxels visualized on top of it (blue and purple, respectively); (B) volumetric rendering of a 3D ROI for the same 3D images. The dashed rectangle in (A) indicates a small ROI magnified in the top-left inset. The solid rectangle in (A) shows the extent in the cross-sectional plane of the 3D ROI rendered in (B). The 3D ROI rendered in (B) consists of 100 slices, including the one shown in (A). Part of the attenuation contrast 3D image is cut away in (B) in order to be able to show the pore and water loss segmented voxels.

voxel value contrast to changes due to drying. For each type of 3D image and at any drying stage, we considered two voxel binary masks: the one for water loss pore voxels and the one for pore voxels characterized by water gain. For each 3D image we computed the contrast-to-noise metric of Eq. (2) with i and j corresponding to the water loss pore voxels and water gain pore voxels, respectively. Table 2 reports the values of such metric for the images. Before drying, both XPCI and XACI images exhibit the same degree of contrast between the two types of regions, while, after drying, the XPCI image shows higher contrast, only slightly perceivable by simple visual comparison of Figures 2(A) and (B). Drying produced a 31.5% increase in that CNR for the XACI images while a 97.5% for the XPCI ones, directly reflected in the fact that only the time-differential XPCI image allows locating unequivocally the changes, while the XACI one does not (Fig. 3).

Table 2. Contrast-to-noise ratio (CNR) between pore voxel regions characterized by water loss and pore regions with water gain. The definition of the CNR is given in Eq. (2), where the indexes i and j refer to the two subpopulations of voxels for any raw 3D image

Type of dataset	Before drying	After drying
XPCI	0.40	0.78
XACI	0.41	0.53

Reliability of the segmentation results

In order to get a qualitative assessment of the in-pore water loss segmentation reliability, from the physics of drying point of view, we needed to evaluate whether (1) the pore segmentation is reliable or not and (2) the in-pore water loss spatial pattern is in agreement with the pore geometrical

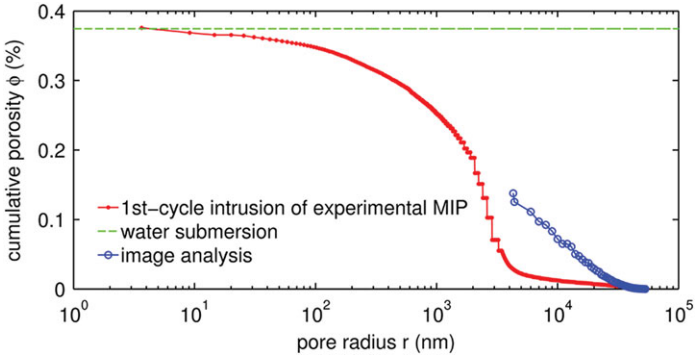

Fig. 7. (colour in the online version). Pore size cumulative distribution (PScD) curves obtained by the first cycle mercury intrusion porosimetry (MIP, solid circles) and by continuous PScD analysis of the segmented pores from the attenuation contrast 3D images (open circles). On the vertical axis the cumulative pore volume divided by the sample volume (cumulative porosity) is plotted. The horizontal, dashed line represents the total open porosity as measured by the water submersion method.

properties. In Figure 7 we have plotted the cumulative pore volume fraction (cumulative pore volume up to a certain pore size level divided by total sample volume, also called cumulative porosity), as a function of the pore size (the radius of the overlapping spheres used to cover the pore volume, according to the 'continuous' PScD method), obtained from the image analysis (open circles) and from the first cycle MIP intrusion measurement (solid circles).

The dashed horizontal line represents the cumulative (open) porosity as obtained by gravimetric measurements on five different Globigerina limestone samples from the same batch of the tomographed sample, measuring their mass before and after submersion in water under low vacuum conditions (5 mbar).

Although MIP can measure the PScD up to the nanometer scale, the curve obtained from the pore segmentation is bound by the spatial resolution (about 5 μm for the equivalent pore radius). As the water absorption measurement shows, the pore volume that can be assessed by X-ray imaging, at the given spatial resolution level, is about only one-third of the total pore volume that water can actually occupy. This means that, in the saturated stage, most of the water occupies pores much smaller than 5 μm in radius.

A clear difference can be seen between the image analysis results and the MIP ones. Such difference is expected since MIP measurements are known to associate larger volume fractions to smaller pore (intrusion) radiuses due to the ink-bottle effect (Kaufmann, 2009). Such effect leads MIP to systematically produce distribution curves which are spuriously laterally shifted towards smaller pore radius values. According to the first cycle intrusion MIP curve of Figure 7, the average pore radius is 1.98 μm, smaller than the spatial resolution and of what one would expect from the image analysis distribution curve. For our sample, the ink-bottle effect was rather strong. See section S6 of Yang *et al.* (2015), for a semiquantitative assessment of the ink-bottle effect degree based upon the two-cycle MIP measurements.

Taking into consideration the ink-bottle effect, the MIP and image analysis pore radius cumulative distribution curves look qualitatively in agreement with each other, leading to more similar values for the average pore radius, allowing us to consider the pore segmentation results as reliable.

As mentioned in section 'Tomographic datasets: processing and analysis', we then used the results of the 'continuous' PScD analysis according to the method proposed by Münch & Holzer (2008), to evaluate the amount of in-pore water loss for each range of the average pore size (radius) r. Figure 8 reports the plot of the water desaturation degree, *DS*, a measure of how much water volume per total pore volume an initially saturated pore region has lost due to drying, as a function of r. The range of r values was divided in a total of 49 bins. For each bin, we counted the number of pores falling in it and computed the respective volume sum.

Figure 8 shows an increase in the desaturation degree with increasing r. The only exception to such monotonic behaviour occurs in the neighbourhood of $r \cong 41$–42 μm, where a drop in desaturation degree occurs in correspondence of one bin. We could not find any reason related to image processing artefacts or specific microstructural properties of the sample for such drop. Thus, we consider such point in the curve of Figure 8 as a statistical outlier. We also observe that with increasing r the fluctuations in the desaturation degree values become larger due to smaller statistics (less large pores).

The trend shown in Figure 8 is expected considering the basic physics of drying in porous media. Water evaporation leads to the formation of air–water menisci interfaces. Such menisci are accompanied by capillary forces which are larger in smaller pores, according to the Young–Laplace equation. As evaporation progresses, the saturated pore space gets increasingly occupied by air via bursts of air invasion following typical patterns of invasion percolation (Wilkinson & Willemsen, 1983). Smaller pores tend to be air-invaded later than larger pores because in addition to air invasion there is water flow, driven by the large spatial gradients in capillary forces,

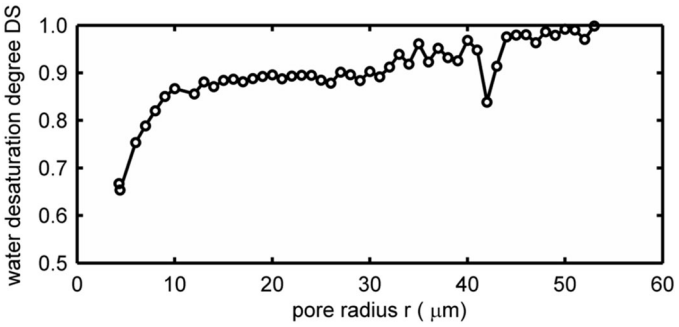

Fig. 8. Water desaturation degree, DS, as a function of the average pore radius as calculated by the 'continuous' pore size cumulative distribution method of Münch & Holzer (2008), applied to the pore 3D binary image and to the in-pore water loss regions segmented from the time-differential phase contrast image.

from the larger pores, with smaller meniscus curvature, to the smaller pores, with larger curvature (Xu *et al.*, 2008). This means that smaller pores are more frequently characterized by a continuous inter-play between emptying (air invasion) and replenishing (water displacement).

The overall expected results is a smaller degree of desaturation for the smaller pores than for the larger ones, at any given drying stage, as observed in our results reported in Figure 8. Thus, the segmentation of water loss regions based upon the time-differential XPCI can be considered physically meaningful, in terms of some of the basic pore-scale drying processes.

Discussion, outlook and conclusions

Figure 3 and the 3D image analysis clearly demonstrate higher sensitivity of XPCI in detecting pore-scale water content changes and in mapping where these changes are located, compared with XACI. This was one of the main targets at the beginning of this work.

Regarding the 3D image analysis, we have focused only on water changes inside segmented pores. From the point of view of the drying investigation, the analysis has allowed distinguishing three categories of water content change regions (Figs. 4A and 5). We have interpreted those categories as water loss, water gain and no water change regions. Such interpretation is driven by what is expected by the physics of drying at the pore scale.

Evaporative drying leads to the gradual substitution of liquid water by air. Even for a configuration as in our experiment, where only one boundary surface is open for vapour transfer to the environment and the sample has large aspect ratio along the direction orthogonal to that surface, the progression of the so-called 'drying front' (the ideal surface separating the part of the sample with almost no water left and the part partially or yet completely saturated) should not be expected to be spatially uniform, with a clear cut distinction between dry regions and partially saturated ones. Rather, as shown in many studies with neutron imaging (Shokri *et al.*, 2009; Shokri & Sahimi, 2012), confocal scanning laser microscopy (Xu *et al.*, 2008) and computational modeling (Prat, 2002; Yiotis *et al.*, 2003), the drying front can either be a very 'rough' and discontinuous surface or can actually be an extended region where percolating air invasion regions (Wilkinson & Willemsen, 1983) are intertwined with small water clusters, mainly associated with small pores (Xu *et al.*, 2008). Such clusters play a relevant role in determining the drying kinetics during the early stage of the process, when a characteristic constant drying rate is typically observed (Lehmann *et al.*, 2008; Or *et al.*, 2013). Such water clusters are thought of supporting hydraulic liquid transport, via capillary forces, from the part of the sample with higher water content (or completely saturated) till the top, evaporating surface. The observation of such clusters in numerical simulations and by neutron imaging (Shokri *et al.*, 2009; Shokri & Sahimi, 2012) is compatible with our identification of water gain regions. Such identification matches also the characterization of the sample drying kinetics by gravimetric measurements performed after the beamtime in similar environmental conditions (temperature and RH) and with the same time interval (see section S7 in Yang *et al.*, 2015 for the results and their analysis). The gravimetric measurements indicate that at the start of the second scan the sample was very likely still within the constant rate drying period, implying the persistence of interconnected water clusters up to the sample top surface. This fact could also help understanding why differences in in-pore water content could be detected only in the time differential XPCI image and not by visual inspection of the two XPCI images separately, due to the lack of complete drying.

We remark that sorting out the in-pore water change regions in three categories leads only to a qualitative classification. As it can be observed in Figure 5, each of the three best fit Gaussian functions has a large overlap with its nearest neighbour, implying the impossibility of a clear-cut distinction between voxels with no water change and voxels with change. However, the water loss and water gain Gaussians

(dot-crossed and dashed lines in Fig. 5, respectively) show almost no overlap, allowing for better distinction between voxels of the two types. Thus, further analysis should focus not only on the spatial distribution of in-pore water loss regions but also on in-pore water gain regions as key players in the capillarity-driven hydraulic transport that support the constant, high drying rate at the beginning of the process.

This work focused on characterizing the potential of XPCI for studying pure water drying in a porous medium. However, the performed measurements (including the two other vertical ROI of the sample scanned), the 3D image analysis results and the developed 3D image analysis workflow allow us for a more complete study of evaporative drying in the investigated limestone. Beyond the analysis of the spatial distribution of water gain regions, work should also focus on water change regions outside of the segmented pores. Such regions may provide information about the part of the pore space below the spatial resolution. As mentioned in the 'Results' section, when the sample is highly saturated, most of water permeates pores which could not be resolved in our 3D images. The use of segmented water change regions outside the segmented pore space was already shown and exploited by Boone *et al.* for analyzing the full pore space of different types of stones (Boone *et al.*, 2014). However, a different segmentation approach for the time-differential XPCI 3D images would be needed for such purpose.

In this work, the drying process was investigated only at two stages because a similar study was performed on a broad range of different porous materials, including mortars. In addition, these experiments were designed to demonstrate the advantages of XPCI over XACI. A new experimental campaign dedicated to imaging water displacement during evaporative drying should include only XPCI and a larger number of successive scans, in order to improve the temporal sampling of the process from a 3D imaging point of view. The scans should be performed by keeping the sample continuously on the X-ray tomographic microscope sample holder, installed inside a small climatic chamber connected with a circuit of air conditioned at a fixed and constant RH and temperature, as used in Derome *et al.* (2011). The first scan (or set of scans, for multiple ROIs along the Z-axis) should be performed with completely wet air, in order to avoid as much as possible any initial drying occurring during the scan(s) time. Then, the air RH should be set to very low levels, equivalently to what we did by moving the sample into the desiccator, in order to drive the evaporative drying. The single scan time could be reduced to less than the 9 min necessary for our measurements, using sCMOS cameras with higher frame rate available at the TOMCAT beamline. However, a suitable trade-off should be found between temporal resolution of the tomographic scan and the achievable dynamic range of the acquired images, in order to fully exploit the advantages of the phase contrast sensitivity to small changes in pore scale (or even subpore scale) water content. In this work, we opted for a camera guaranteeing larger dynamic range at the cost of smaller temporal resolution.

The same considerations about trade-off between sensitivity to pure water changes and temporal resolution apply to XPCI of other water transport processes. FSP-XPCI performed with synchrotron radiation can provide an alternative to standard XACI of processes faster than drying, e.g. capillary imbibition or drainage, without the need of substituting pure water with solutions containing contrast agents, a strict necessity when dealing with reactive transport mechanisms as those occurring in cement-based materials or in polymer electrolyte membrane fuel cells. This possibility is reinforced by recent advancements in the field of phase retrieval algorithms requiring radiographic acquisition at no more than one or two sample-to-detector distances (Langer *et al.*, 2008; Davidoiu *et al.*, 2011; Moosmann *et al.*, 2011; Mokso *et al.*, 2013), which speeds up the overall tomographic acquisition procedure.

In conclusion, we have performed XTM measurements with synchrotron radiation on a limestone sample at two different saturation stages during its drying, with two different sample-to-detector distances in order to be able to produce two sets of 3D images with distinct contrast, either based upon X-ray attenuation or refraction (phase shift). We could identify water content change regions only in the time-differential phase contrast images, demonstrating that XPCI can empower the pore-scale 3D visualization of water spatio-temporal distribution during transport processes, thus avoiding the need of contrast agents added to the water, as typically used in XACI. The 3D image analysis of the phase contrast images allowed us obtaining some features of the pore-scale drying process in agreement with what observed with other microscopy techniques, computational modelling results and the basic theory of drying in porous media. The results of this work suggest that XPCI provides new opportunities for any investigation where it is needed to visualize pure water in a porous material, especially in the case of reactive water transport processes.

Acknowledgements

We acknowledge the support of the Swiss National Science Foundation (project nr. 200021_143782), of the Swiss Light Source (SLS), Paul Scherrer Institute (PSI) (beamtime project nr. 20140234) and of the Helmholtz Virtual Institute for New X-ray analytic Methods in Materials science (VI-NXMM). We would like to thank Julia Herzen, Technical University Munich, Alex Hipp, Fabian Wilde, Pavel Lytaev and Imke Grevin, Helmholtz Center for Materials and Coastal Research and DESY, for allowing and supporting us in performing preliminary free-space propagation XPCI tests on our samples during their beamtime at DESY. We would like to thank Gordan Mikuljan, X-ray Tomography Group, SLS, PSI, for helping with the preparation of the synchrotron radiation beamtime, Elisa Franzoni, University of Bologna, for supplying

the Globigerina limestone batches, Mateusz Wyrzykowski, Concrete/Construction Chemistry Laboratory, Empa, for helping setting up the mercury intrusion porosimetry measurements, Roger Vonbank and Stephan Carl, Laboratory for Multiscale Studies in Building Physics, Empa, for making available their climatic chamber for testing drying protocols and Nikolajs Toropovs, Riga Technical University, for helping with the sample preparation. Finally, we would like to thank the three anonymous reviewers for useful suggestions which helped improving the article.

References

Andrew, M., Bijeljic, B. & Blunt, M.J. (2013) Pore-scale imaging of geological carbon dioxide storage under in situ conditions. *Geophys. Res. Lett.* **40**, 3915–3918.

Andrew, M., Bijeljic, B. & Blunt, M.J. (2014) Pore-by-pore capillary pressure measurements using X-ray microtomography at reservoir conditions: curvature, snap-off, and remobilization of residual CO_2. *Water Res. Res.* **50**, 8760–8774.

Armstrong, R.T., Georgiadis, A., Ott, H., Klemin, D. & Berg, S. (2014a) Critical capillary number: desaturation studied with fast X-ray computed microtomography. *Geophys. Res. Lett.* **41**, 55–60.

Armstrong, R.T., Ott, H., Georgiadis, A., Rücker, M., Schwing, A. & Berg, S. (2014b) Subsecond pore-scale displacement processes and relaxation dynamics in multiphase flow. *Water Res. Res.* **50**, 9162–9176.

Attix, F.H. (1986) *Introduction to Radiological Physics and Radiation Physics*, Wiley, New York. Chapter 7, Fig. 7.1, p. 125.

Banhart, J. (ed.) (2008) *Advanced Tomographic Methods in Materials Research and Engineering*. Oxford University Press. Oxford, UK.

Bazylak, A. (2009) Liquid water visualization in PEM fuel cells: a review. *Int. J. Hydr. Energy* **34**, 3845–3857.

Beltran, M.A., Paganin, D.M., Uesugi, K. & Kitchen, M.J. (2010) 2D and 3D X-ray phase retrieval of multi-material objects using a single defocus distance. *Optics Expr.* **18**, 6423–6436.

Berg, S., Ott, H., Klapp, S.A., *et al.* (2013) Real-time 3D imaging of Haines jumps in porous media flow. *Proc. Natl. Acad. Sci.* **110**, 3755–3759.

Bonse, U. & Hart, M. (1965) An X-ray interferometer. *Appl. Phys. Lett.* **6**, 155–156.

Boone, M.A., De Kock, T., Bultreys, T., De Schutter, G., Vontobel, P., Van Hoorebeke, L. & Cnudde, V. (2014) 3D mapping of water in oolithic limestone at atmospheric and vacuum saturation using X-ray micro-CT differential imaging. *Mat. Charact.* **97**, 150–160.

Boone, M.N., Devulder, W., Dierick, M., Brabant, L., Pauwels, E. & Van Hoorebeke, L. (2012) Comparison of two single-image phase-retrieval algorithms for in-line x-ray phase-contrast imaging. *J. Opt. Soc. Amer. A* **29**, 2667–2672.

Bravin, A. (2003) Exploiting the X-ray refraction contrast with an analyser: the state of the art. *J. Phys. D Appl. Phys.* **36**, A24–A29.

Brown, K., Schlüter, S., Sheppard, A. & Wildenschild, D. (2014) On the challenges of measuring interfacial characteristics of three-phase fluid flow with x-ray microtomography. *J. Microsc.* **253**, 171–182.

Bultreys, T., Boone, M.A., Boone, M.N., De Schryver, T., Masschaele, B., Van Hoorebeke, L. & Cnudde, V. (2015) Fast laboratory-based micro-computed tomography for pore-scale research: illustrative experiments and perspectives on the future. Adv. Water Res. doi: 10.1016/j.advwatres.2015.05.012.

Burvall, A., Lundström, U., Takman, P.A., Larsson, D.H. & Hertz, H.M. (2011) Phase retrieval in X-ray phase-contrast imaging suitable for tomography. *Optics Expr.* **19**, 10359–10376.

Cassar, J. (2002) Deterioration of the Globigerina limestone of the Maltese Islands. *Geol. Soc. London Spec. Publ.* **205**, 33–49.

Chapman, D., Thomlinson, W., Johnston, R.E., *et al.* (1997) Diffraction enhanced x-ray imaging. *Phys. Med. Biol.* **42**, 2015–2025.

Choi, C., Balcom, B.J., Beyea, S.D., Bremner, T.W., Grattan-Bellew, P.E. & Armstrong, R.L. (2000) Spatially resolved pore-size distribution of drying concrete with magnetic resonance imaging. *J. Appl. Phys.* **88**, 3578–3581.

Clauser, J.F. & Reinsch, M.W. (1992) New theoretical and experimental results in Fresnel optics with applications to matter-wave and X-ray interferometry. *Appl. Phys. B.* **54**, 380–395.

Cloetens, P., Pateyron-Salome, M., Byffiere, J.-Y., Peix, G., Baruchel, J., Peyrin, F. & Schlenker, M. (1997) Observation of microstructure and damage in materials by phase sensitive radiography and tomography. *J. Appl. Phys.* **81**, 5878–86.

Cloetens, P., Ludwig, W., Baruchel, J., Van Dyck, D., Van Landuyt, J., Guigay, J.P. & Schlenker, M. (1999) Holotomography: quantitative phase tomography with micrometer resolution using hard synchrotron radiation x rays. *Appl. Phys. Lett.* **75**, 2912–2914.

Dann, R., Turner, M., Close, M. & Knackstedt, M. (2011) Multi-scale characterisation of coastal sand aquifer media for contaminant transport using X-ray computed tomography. *Env. Earth Sci.* **63**, 1125–1137.

Davidoiu, V., Sixou, B., Langer, M. & Peyrin, F. (2011) Non-linear iterative phase retrieval based on Frechet derivative. *Optics Expr.* **19**, 22809–22819.

Dempster, A.P., Laird, N.M. & Rubin, D.B. (1977) Maximum likelihood from incomplete data via the EM algorithm. *J. Royal Stat. Soc. B.* **39**, 1–22.

Derluyn, H., Dewanckele, J., Boone, M.N., Cnudde, V., Derome, D. & Carmeliet, J. (2014) Crystallization of hydrated and anhydrous salts in porous limestone resolved by synchrotron X-ray microtomography. *Nucl. Instr. Meth. Phys. Res. B.* **324**, 102–112.

Derome, D., Griffa, M., Koebel, M. & Carmeliet, J. (2011) Hysteretic swelling of wood at cellular scale probed by phase-contrast X-ray tomography. *J. Struct. Biol.* **173**, 180–190.

Endrizzi, M., Diemoz, P.C., Millard, T.P., Louise Jones, J., Speller, R.D., Robinson, I.K. & Olivo, A. (2014). *Appl. Phys. Lett.* **104**, 1–4.

Faure, P.F., Caré, S., Magat, J. & Chaussadent, T. (2012) Drying effect on cement paste porosity at early age observed by NMR methods. *Constr. Build. Mat.* **29**, 496–503.

Franzoni, E. Sassoni, E., Scherer, G.W. & Naidu, S. (2013) Artificial weathering of stone by heating. *J. Cult. Herit.* **14**, e85–e93.

Franzoni, E., Graziani, G., Sassoni, E., Bacilieri, G., Griffa, M. & Lura, P. (2014) Solvent-based ethyl silicate for stone consolidation: influence of the application technique on penetration depth, efficacy and pore occlusion. *Mat. Struct.* doi: 10.1617/s11527-014-0417-1.

Furuberg, L., Feder, J., Aharony, A. & Jøssang, T. (1988) Dynamics of invasion percolation. *Phys. Rev. Lett.* **61**, 2117–2120.

Ghous, A., Senden, T.J., Sok, R.M., *et al.* (2007) 3D characterization of microporosity in carbonate cores. *SPWLA Middle East Regional Symposium*. pp. 15–19.

Gureyev, T.E., Mayo, S.C., Myers, D.E., Nesterets, Y., Paganin, D.M., Pogany, A., Stevenson, A.W. & Wilkins, S.W. (2009) Refracting Röntgen's rays: propagation-based x-ray phase contrast for biomedical imaging. *J. Appl. Phys.* **105**, 1–12.

Henke, B.L., Gullikson, E.M. & Davis, J.C. (1993) X-ray interactions: photoabsorption, scattering, transmission, and reflection at E = 50-30000 eV, Z = 1-92. *Atom. Data Nucl. Data Tables.* **54**, 181–343. http://henke.lbl.gov/optical_constants/

Irvine, S., Mokso, R., Modregger, P., Wang, Z., Marone, F. & Stampanoni, M. (2014) Simple merging technique for improving resolution in qualitative single image phase contrast tomography. *Optics Expr.* **22**, 27257–27269.

Jain, A.K., Murty, M.N. & Flynn, P.J. (1999) Data clustering: a review. *ACM Comp. Surv.* **31**, 264–323.

Kaestner, A., Hassanein, R., Vontobel, P., Lehmann, P., Schaap, J., Lehmann, E. & Fluhler, H. (2007) Mapping the 3D water dynamics in heterogeneous sands using thermal neutrons. *Chem. Eng. J.* **130**, 79–85.

Kaestner, A., Münch, B., Trtik, P. & Butler, L. (2011) Spatiotemporal computed tomography of dynamic processes. *Opt. Eng.* **50**, 123201–123201.

Kanungo, T., Mount, D.M., Netanyahu, N.S., Piatko, C.D., Silverman, R. & Wu, A.Y. (2002) An efficient k-means clustering algorithm: analysis and implementation. *IEEE Tran.s Patt. Anal. Machine Intell.* **24**, 881–892.

Kaufmann, J., Loser, R. & Leemann, A. (2009) Analysis of cement-bonded materials by multi-cycle mercury intrusion and nitrogen sorption. *J. Colloid. Interf. Sci.* **336**, 730–737.

Ketcham, R.A. & Iturrino, G.J. (2005) Nondestructive high-resolution visualization and measurement of anisotropic effective porosity in complex lithologies using high-resolution X-ray computed tomography. *J. Hydr.* **302**, 92–106.

Kohout, M., Grof, Z. & Štěpánek, F. (2006) Pore-scale modelling and tomographic visualisation of drying in granular media. *J. Coll. Interf. Sci.* **299**, 342–351.

Langer, M., Cloetens, P., Guigay, J.-P. & Peyrin, F. (2008) Quantitative comparison of direct phase retrieval algorithms in in-line phase tomography. *Med. Phys.* **35**, 4556–4566.

Le Bray, Y. & Prat, M. (1999) Three-dimensional pore network simulation of drying in capillary porous media. *Int. J. Heat Mass Transf.* **42**, 4207–4224.

Lee, S.-J. & Kim, Y. (2008) In vivo visualization of the water-refilling process in xylem vessels using X-ray micro-imaging. *Ann. Bot.* **101**, 595–602.

Leemann, A. & Loser, R. (2011) Analysis of concrete in a vertical ventilation shaft exposed to sulfate-containing groundwater for 45years. *Cem. Concr. Comp.* **33**, 74–83.

Lehmann, P., Assouline, S. & Or, D. (2008) Characteristic lengths affecting evaporative drying of porous media. *Phys. Rev. E* **77**, 1–16.

Lura, P., Pease, B., Mazzotta, G.B., Rajabipour, F. & Weiss, J. (2007) Influence of shrinkage-reducing admixtures on development of plastic shrinkage cracks. *ACI Mat. J.* **104**, 187–194.

MacQueen, J. (1967) Some methods for classification and analysis of multivariate observations. *Proceed. Fifth Berkeley Symp. Math. Stat. Prob.* **1**, 281–297.

Marone, F. & Stampanoni, M. (2012) Regridding reconstruction algorithm for real-time tomographic imaging. *J. Synchr. Rad.* **19**, 1029–1037.

Mayo, S.C., Stevenson, A.W. & Wilkins, S.W. (2012) In-line phase-contrast X-ray imaging and tomography for materials science. *Materials* **5**, 937–965.

Mitchell, J., Chandrasekera, T.C., Holland, D.J., Gladden, L.F. & Fordham, E.J. (2013) Magnetic resonance imaging in laboratory petrophysical core analysis. *Phys. Rep.* **526**, 165–225.

Mokso, R., *et al.* (2013) Advantages of phase retrieval for fast x-ray tomographic microscopy. *J. Phys. D: Appl. Phys.* **46**, 1–12.

Momose, A. (1995) Demonstration of phase-contrast X-ray computed tomography using an X-ray interferometer. *Nucl. Instr. Meth. Phys. Res. A* **352**, 622–628.

Momose, A., Takeda, T., Itai, Y. & Hirano, K. (1996) Phase-contrast X-ray computed tomography for observing biological soft tissues. *Nat. Med.* **2**, 473–475.

Moosmann, J., Hofmann, R. & Baumbach, T. (2011) Single-distance phase retrieval at large phase shifts. *Optics Expr.* **19**, 12066–12073.

Munro, P.R., Ignatyev, K., Speller, R.D. & Olivo, A. (2012) Phase and absorption retrieval using incoherent X-ray sources. *Proc. Nat. Acad. Sci.* **109**, 13922–13927.

Münch, B. (2014) Empa Bundle of ImageJ Plugins for Image Analysis (EBIPIA). http://wiki.imagej.net/Xlib

Münch, B. & Holzer, L. (2008) Contradicting geometrical concepts in pore size analysis attained with electron microscopy and mercury intrusion. *J. Am. Ceram. Soc.* **91**, 4059–4067.

Myers, G.R., Kingston, A.M., Varslot, T.K., Turner, M.L. & Sheppard, A.P. (2011) Dynamic tomography with a priori information. *Appl. Optics* **50**, 3685–3690.

Nakashima, Y. (2013) The use of sodium polytungstate as an X-ray contrast agent to reduce the beam hardening artifact in hydrological laboratory experiments. *J. Hydr. Hydromech.* **61**, 347–351.

Nakashima, Y. & Nakano, T. (2012) Nondestructive quantitative analysis of a heavy element in solution or suspension by single-shot computed tomography with a polychromatic X-ray source. *Anal. Sci.* **28**, 1133–1138.

Nakashima, Y. & Nakano, T. (2014) Optimizing contrast agents with respect to reducing beam hardening in nonmedical X-ray computed tomography experiments. *J. X-ray Sci. Tech.* **22**, 91–103.

Norouzi Rad, M. & Shokri, N. (2014) Effects of grain angularity on NaCl precipitation in porous media during evaporation. *Water Res. Res.* **50**, 9020–9030.

Norouzi Rad, M., Shokri, N. & Sahimi, M. (2013) Pore-scale dynamics of salt precipitation in drying porous media. *Phys. Rev. E* **88**, 1–5.

Nugent, K.A., Gureyev, T.E., Cookson, D.F., Paganin, D. & Barnea, Z. (1996) Quantitative phase imaging using hard x rays. *Phys. Rev. Lett.* **77**, 2961–2964.

Olivo, A., Bohndiek, S.E., Griffiths, J.A., Konstantinidis, A. & Speller, R.D. (2009) A non-free-space propagation x-ray phase contrast imaging method sensitive to phase effects in two directions simultaneously. *Appl. Phys. Lett.* **94**, 1–3.

Olivo, A. & Speller, R. (2007) A coded-aperture technique allowing x-ray phase contrast imaging with conventional sources. *Appl. Phys. Lett.* **91**, 1–3.

Or, D., Lehmann, P., Shahraeeni, E. & Shokri, N. (2013) Advances in soil evaporation physics—a review. *Vadose Zone J.* **12**, 1–16.

Paganin, D., Mayo, S.C., Gureyev, T.E., Miller, P.R. & Wilkins, S.W. (2002) Simultaneous phase and amplitude extraction from a single defocused image of a homogeneous object. *J. Microsc.* **206**, 33–40.

Paganin, D.M. (2006) *Coherent X-ray Optics*. Oxford University Press, Oxford , UK.

Pease, B.J., Scheffler, G.A. & Janssen, H. (2012) Monitoring moisture movements in building materials using X-ray attenuation: influence of beam-hardening of polychromatic X-ray photon beams. *Constr. Build. Mat.* **36**, 419–429.

Pel, L. & Huinink, H.P. (2012) Building materials studied by MRI. *Encyclopedia of Magnetic Resonance* (ed. by R. K. Harris), pp. 873–882. John Wiley & Sons Ltd., Chichester, UK.

Perfect, E., Cheng, C.-L., Kang, M., Bilheux, H.Z., Lamanna, J.M., Gragg, M.J. & Wright, D.M. (2014) Neutron imaging of hydrogen-rich fluids in geomaterials and engineered porous media: a review. *Earth Sci. Rev.* **129**, 120–135.

Pfeiffer, F., Weitkamp, T., Bunk, O. & David, C. (2006) Phase retrieval and differential phase-contrast imaging with low-brilliance X-ray sources. *Nat. Phys.* **2**, 258–261.

Prat, M. (2002) Recent advances in pore-scale models for drying of porous media. *Chem. Eng. J.* **86**, 153–164.

Prime, N., Housni, Z., Fraikin, L., Léonard, A., Charlier, R. & Levasseur, S. (2015) On water transfer and hydraulic connection layer during the convective drying of rigid porous material. *Transp. Por. Media* **106**, 47–72.

Roughan. (2009). http://www.mathworks.com/matlabcentral/fileexchange/24867-gaussianmixturemodel-m/content/gaussian_mixture_model.m

Sant, G. & Weiss, J. (2009) Using X-ray absorption to assess moisture movement in cement-based materials. *J. ASTM Int.* **6**, JAI102234.

Schaap, J.D., Lehmann, P., Kaestner, *et al.* (2008) Measuring the effect of structural connectivity on the water dynamics in heterogeneous porous media using speedy neutron tomography. *Adv. Wat. Res.* **31**, 1233–1241.

Scherer, G.W. (1990) Theory of drying. *J. Amer. Cer. Soc.* **73**, 3–14.

Schindelin, J., *et al.* (2012) Fiji: an open-source platform for biological-image analysis. *Nature Meth.* **9**, 676–682.

Shokri, N., Lehmann, P. & Or, D. (2009) Critical evaluation of enhancement factors for vapor transport through unsaturated porous media. *Water Res. Res.* **45**, 1–9.

Shokri, N. & Sahimi, M. (2012) Structure of drying fronts in three-dimensional porous media. *Phys. Rev. E* **85**, 1–8.

Stampanoni, M., Mokso, R., Marone, F., Vila-Comamala, J., Gorelick, S., Trtik, P., Jefimovs, K. & David, C. (2010) Phase-contrast tomography at the nanoscale using hard x rays. *Phys. Rev. B* **81**, 1–4.

Torquato, S. (2002) *Random Heterogeneous Materials*. Sections 2.6 and 12.5.4. Springer-Verlag, New York.

Valckenborg, R.M.E., Pel, L., Hazrati, K., Kopinga, K. & Marchand, J. (2001) Pore water distribution in mortar during drying as determined by NMR. *Mat. Struct.* **34**, 599–604.

Wang, Y., Chen, K.S., Mishler, J., Cho, S.C. & Adroher, X.C. (2011) A review of polymer electrolyte membrane fuel cells: technology, applications, and needs on fundamental research. *Appl. Energy* **88**, 981–1007.

Wang, Y., Kharaghani, A., Metzger, T. & Tsotsas, E. (2012) Pore network drying model for particle aggregates: assessment by X-ray microtomography. *Drying Tech.* **30**, 1800–1809.

Weitkamp, T., Diaz, A., David, C., Pfeiffer, F., Stampanoni, M., Cloetens, P. & Ziegler, E. (2005) X-ray phase imaging with a grating interferometer. *Opt. Express* **13**, 6296–6304.

Weitkamp, T., Haas, D., Wegrzynek, D. & Rack, A. (2011) ANKAPhase: software for single-distance phase retrieval from inline X-ray phase-contrast radiographs. *J. Synchr. Rad.* **18**, 617–629.

Wildenschild, D., Vaz, C.M.P., Rivers, M.L., Rikard, D. & Christensen, B.S.B. (2002) Using X-ray computed tomography in hydrology: systems, resolutions, and limitations. *J. Hydr.* **267**, 285–297.

Wildenschild, D. & Sheppard, A.P. (2013) X-ray imaging and analysis techniques for quantifying pore-scale structure and processes in subsurface porous medium systems. *Adv. Water Res.* **51**, 217–246.

Wilkinson, D. & Willemsen, J.F. (1983) Invasion percolation: a new form of percolation theory. *J. Phys. A Math. Gen.* **16**, 3365–3376.

Xu, L., Davies, S., Schofield, A. & Weitz, D. (2008) Dynamics of drying in 3D porous media. *Phys. Rev. Lett.* **101**, 1–4.

Yang, F., Prade, F., Griffa, M., Jerjen, I., Sarapata, A., Herzen, J., Pfeiffer, F. & Lura, P. (2014) Dark-field X-ray imaging of water unsaturated transport in porous materials. *Appl. Phys. Lett.* **105**, 1–5.

Yang, F., *et al.* (2015) Supplementary Materials available at http://www.calcolodistr.altervista.org/en/work/sunto/FYangEtAl_XPCIPureWater_SupplMats_v2_final.pdf.

Ye, G. (2003) Experimental study and numerical simulation of the development of the microstructure and permeability of cementitious materials. PhD Thesis, Delft Technical University.

Yiotis, A., Boudouvis, A., Stubos, A., Tsimpanogiannis, I. & Yortsos, Y. (2003) Effect of liquid films on the isothermal drying of porous media. *Phys. Rev. E* **68**, 1–4.

Youssef, S., Deschamps, H., Dautriat, J., Rosenberg, E., Oughanem, R., Maire, E. & Mokso, R. (2013) 4D imaging of fluid flow dynamics in natural porous media by ultra-fast x-ray microtomography. *Int. Symp. SCA*, **176**. Napa Valley, California. 1–12.

Supporting Information

Additional Supporting information may be found in the online version of this article at the publisher's website:

Fig. S1. Plot of the ratio between the decrement δ of the real part of the index of refraction and its imaginary part β as a function of the photon energy E.

Fig. S2. Individual plots of the decrement δ of the real part (inset (a)) and the imaginary part β (inset (b) of the index of refraction n for the same photon energy E as in Fig. S1.

Fig. S3. Overlapping of the 1st slice of the *XACI* 3D image after drying (grey tones) and of the corresponding slice of the pore 3D binary image (semi-transparent blue color), the latter obtained by *k*-means clustering of the two XACI 3D images with a 1D feature space based on the voxel value only.

Fig. S4. Voxel value, V_0, cumulative distribution functions (CDFs) for the XPCI ((a)) and XACI ((b)) 3D images, before (blue curve) and after (red curve) drying. $P(V \leq V_0)$ means the probability for the event $V \leq V_0$, where V indicates generically the voxel value as a random variable.

Fig. S5. Voxel value histograms the CDFs of Fig. S4 are derived from. (a) and (b): XPCI 3D images, before and after drying, respectively. (c) and (d): XACI 3D images, before and after drying, respectively.

Fig. S6. Voxel value cumulative distribution functions (CDFs) for the raw XPCI (a) and XACI (b) 3D images, with the blue

line indicating the image before drying while the red line after drying.

Fig. S7. Voxel value histograms the CDFs of Fig. S6 are derived from. (a) and (b): XPCI 3D images, before and after drying, respectively. (c) and (d): XACI 3D images, before and after drying, respectively.

Fig. S8. Voxel value histogram (open circles) from the time-differential XPCI 3D image considering only the segmented pore voxels. 2-Gaussian mixture best fit using the expectation maximization (EM) method.

Fig. S9. Comparison between pore size (complementary) cumulative distribution functions obtained by 2-cycle mercury intrusion porosimetry and 3D image analysis. The red curve refers to the first cycle intrusion and is the same one reported in Fig. 7 within the article.

Fig. S10. Drying rate, e, time series measured during a drying experiment with the same sample used during the beamtime but performed after the beamtime, in environmental and loading conditions similar to those occurred during the beamtime itself. During the first 1.5 hours, the sample was kept at about 50% RH and 23°C.

Fig. S11. Vertical (Y-Z) slice from the dried XACI dataset, taken in the middle of the sample, with the segmented pore and water loss voxels visualized on top of it (blue and purple, respectively).

Table SI: Values for three different goodness-of-fit metrics applied to the best fit of the voxel value histogram of the time-differential XPCI 3D image, considering only voxels belonging to the pore region, and using two best fit models, a 2-Gaussian mixture and a 3-Gaussian one.